



Assessing the high concentration of vacancies in refractory high entropy alloys

Wilson, Jack A.; Moore, Christopher; Goddard, David T.; Middleburgh, Simon C.

Materialia

DOI:
[10.1016/j.mtla.2023.101764](https://doi.org/10.1016/j.mtla.2023.101764)

Published: 01/05/2023

Peer reviewed version

[Cyswllt i'r cyhoeddiad / Link to publication](#)

Dyfyniad o'r fersiwn a gyhoeddwyd / Citation for published version (APA):
Wilson, J. A., Moore, C., Goddard, D. T., & Middleburgh, S. C. (2023). Assessing the high concentration of vacancies in refractory high entropy alloys. *Materialia*, 28, Article 101764. <https://doi.org/10.1016/j.mtla.2023.101764>

Hawliau Cyffredinol / General rights

Copyright and moral rights for the publications made accessible in the public portal are retained by the authors and/or other copyright owners and it is a condition of accessing publications that users recognise and abide by the legal requirements associated with these rights.

- Users may download and print one copy of any publication from the public portal for the purpose of private study or research.
- You may not further distribute the material or use it for any profit-making activity or commercial gain
- You may freely distribute the URL identifying the publication in the public portal ?

Take down policy

If you believe that this document breaches copyright please contact us providing details, and we will remove access to the work immediately and investigate your claim.

Assessing the high concentration of vacancies in refractory high entropy alloys

Jack A. Wilson^{1*}, Christopher Moore¹, David T. Goddard², Simon C. Middleburgh¹,

¹Nuclear Futures Institute, Bangor University, Bangor, LL57 1UT, United Kingdom

²National Nuclear Laboratory, Preston Laboratory, Springfields, Preston, Lancashire PR4 0XJ, United Kingdom

* Author to whom correspondence should be addressed

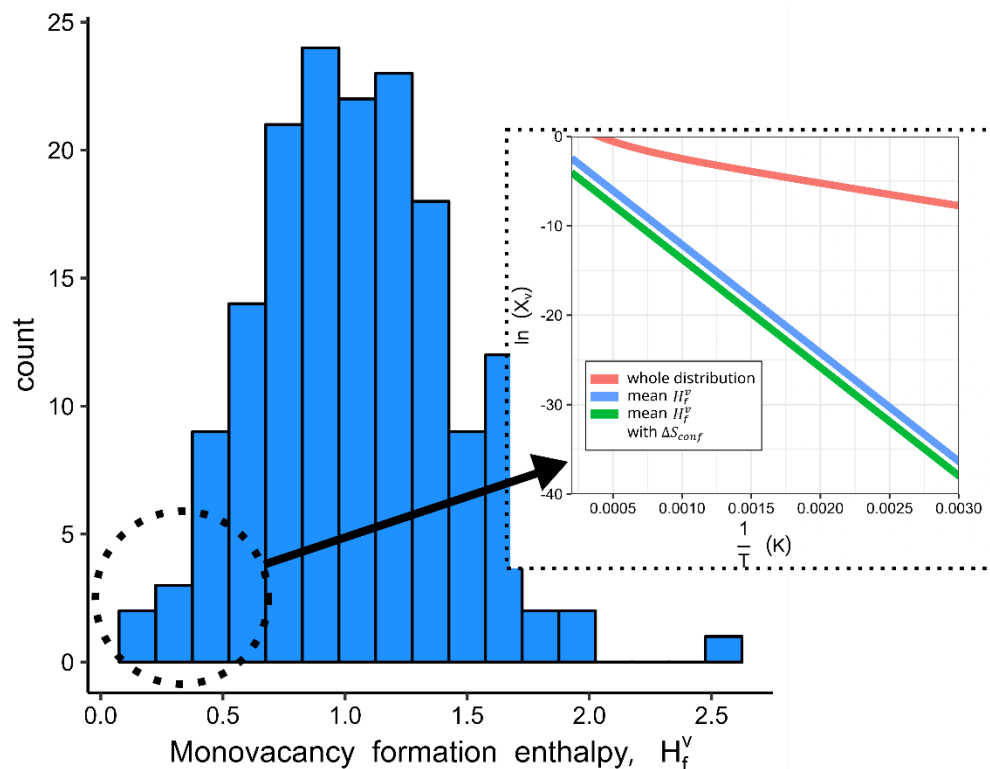
Email: * jack.wilson@bangor.ac.uk; jackwilson.mchem@gmail.com.

Title: Assessing the high concentration of vacancies in refractory high entropy alloys

Journal: Acta Materialia

Keywords: vacancy formation energy; high entropy alloy; defect formation; atomistic modelling

Graphical abstract



20

21 **Abstract**

22 Accurate determination of monovacancy formation enthalpy is vital for work on diffusion, melting
23 point determination of high temperature materials, radiation damage, and thermophysical stability of
24 alloys. These enthalpies take on a single value in pure metals but is made more complex in
25 concentrated solid solutions due to the local chemical environments possible around each vacancy.
26 Herein, using first-principles density functional theory, we report the distributions of vacancy
27 formation enthalpies in 21 equiatomic 5-component solid-solution alloys from the Hf-Mo-Nb-Ta-Ti-
28 W-Zr system. Chemical disorder is treated using the special quasi-random structure method, and the
29 chemical potential of vacant element is treated by approximating it to its total energy in its standard
30 state. We find that the highest vacancy formation enthalpies belong to the MoNbTaTiW alloy (which
31 incidentally is the most reported in literature) and the lowest belongs to HfNbTaTiZr, with other alloys
32 in-between. We use the whole distribution of formation enthalpies to estimate the equilibrium
33 concentration of vacancies as a function of temperature.

34

35 **1. Introduction**

36 High entropy alloys (HEAs), sometimes referred to as compositionally complex alloys, multicomponent
37 element alloys, or concentrated solid solutions, pioneered by Cantor *et al.* [1] and Yeh *et al.* [2], offer
38 innovative multi-component alloy compositions for extreme environment materials such as in the
39 nuclear [3,4] or aerospace [5] industries. Originally defined as having 5 or more elements in high
40 concentrations (5 – 35 at%) [2], high entropy alloys could offer superior properties, including strength
41 and hardness [6,7], oxidation resistance [8–11], and high thermal stability [12]. Vacancies, their
42 formation energies, and their equilibrium concentration have been studied for their role in diffusion
43 kinetics [13], precipitation [14], radiation resistance [13,15,16], and material properties such as
44 strength [17,18]. HEAs are observed to have higher concentrations of vacancy defects compared to
45 conventional alloys [18,19]. The exact mechanism behind this higher concentration is not yet fully
46 understood.

47 Wang *et al.* presented a thermodynamic analysis which concludes that configurational entropy causes
48 a substantial increase in equilibrium vacancy concentrations in high entropy alloys compared to pure
49 metals and binary alloys [19]. Contrary to this, Daigle *et al.* propose that configurational entropy
50 reduces the equilibrium vacancy concentration in high entropy materials [20]. This viewpoint is
51 supported by Jodi *et al.*, who demonstrated that alloys with higher configurational entropy in the
52 $\text{Fe}_x(\text{CoCrMnNi})_{100-x}$ system had lower equilibrium concentrations of monovacancies, although the
53 authors attributed this to the compositional effect of Fe on the vacancy formation enthalpy [21].
54 Daigle *et al.* suggests that most equilibrium vacancies in high entropy materials are produced from the
55 lower tails of the vacancy formation enthalpy distribution, which tend to be significantly lower than
56 the mean. This results in an enhanced vacancy concentration in complex materials such as HEAs,
57 compared to conventional alloys and pure metals [20].

58 Experimental research on vacancy formation in HEAs predominantly relies on positron annihilation
59 lifetime spectroscopy [21,22] and tracer diffusion experiments [23], but presently, few of these studies
60 have been performed. To support experimental efforts, recent advances in density functional theory
61 [24,25], molecular dynamics [26], and machine learning models [27] have enabled the study of
62 vacancy formation in compositionally complex alloys such as HEAs. Many previous studies on vacancy
63 formation enthalpies of compositionally complex alloys have focussed on the Cantor alloy [28] and

64 derivative alloys thereof [22,25,29–34], although studies on some refractory alloys do exist [24,35–
65 38]. For example, Cunliffe *et al.* proposed a method to calculate the vacancy formation enthalpy in
66 multi-component amorphous alloys, including refractory alloys, which involves averaging the vacancy
67 formation enthalpy of the respective pure metals [37]. Roy *et al.* determined the vacancy formation
68 energy of $(\text{Mo}_{0.95}\text{W}_{0.05})_{0.85}\text{Ta}_{0.10}(\text{TiZr})_{0.05}$ via density functional theory to be between 2.87 – 3.84 eV
69 [35]. Zhang *et al.* investigated vacancy energetics in the Al-Hf-Sc-Ti-Zr system, including the binary to
70 quaternary alloys. From this, they calculated the temperature dependence of the Gibbs energy of
71 vacancy formation [24]. Zhao *et al.* determined the vacancy formation enthalpy of CrTaVW to be
72 between 2.45 – 3.94 eV, with a mean value of 3.18 eV [39]. The literature however remains sparse on
73 thorough interrogations of vacancy formation enthalpies in refractory HEAs.

74 Using density functional theory, we examine the vacancy formation enthalpies of all quinary alloys in
75 the seven-element Hf-Mo-Nb-Ta-Ti-W-Zr system. The formation enthalpies of vacancies and their
76 trends are presented. We show that refractory solid solutions have higher equilibrium vacancy
77 concentrations than pure elements, which is not attributed to their increased configurational entropy.
78 Rather, vacancy formation energies at the lower-end tail of the distribution are responsible for the
79 higher equilibrium vacancy concentrations observed in high entropy alloys. These findings suggest
80 important phenomena that may occur in the migration of species (e.g., oxygen and hydrogen), bubble
81 formation and phase segregation and other equilibrium processes in high entropy alloys,
82 compositionally complex alloys, and alloys in general.

83

84 **2. Methodology**

85 *2.1. Special quasi-random structure supercells.*

86 Density functional theory [40,41] is computationally intensive (generally limited to hundreds of atoms
87 at a time). The conventional way to capture bulk material properties is to use periodic boundary
88 conditions, but this imposes non-random periodicity on simulations, which poses challenges for
89 modelling infinitely random lattices in density functional theory computations. Special quasi-random
90 structures (SQS) attempt to replicate random materials by matching correlation functions between
91 pairs of atoms within a defined cut-off radius (short-range interactions are more dominant than long-
92 range interactions) to capture bulk random lattice features. In this study, special quasi-random
93 structures were constructed using the mcsqs code in the Alloy Theoretic Automated Toolkit [42]
94 similar to previous work [38]. We set cut-off distances to include up to third nearest neighbour pair
95 interactions. We did not consider triplet and higher order interactions.

96 *2.2. Total energy Relaxations*

97 Density function theory [40,41] structural relaxation calculations at constant pressure were based on
98 the plane wave pseudopotential approach as implemented in the Vienna *ab initio* simulation package
99 VASP [43,44] version 5.4.4. Projector augmented-wave (PAW) pseudopotentials are used [45,46].
100 Electrons treated as valence are: Hf: 10, Mo: 14, Nb: 13, Ta: 11, Ti: 12, W: 12, and Zr: 12. The Perdew,
101 Burke, and Ernzerhof version of the generalised gradient approximation exchange-correlation
102 functional was applied [47]. Cut-off energy for plane waves were set to 500 eV for all calculations. A
103 Methfessel-Paxton smearing width of 2 eV was used [48]. A K-point mesh was selected based on
104 convergence of the total energy to 0.01 eV/atom which resulted in a $4 \times 4 \times 4$ Γ -centred mesh for
105 all cells. Convergence testing for plane wave cut off energies and K-points can be found in
106 **Supplementary Figures S1-2.**

107 *2.3. Calculating local Bias*

108 We adopt a measure for how the immediate environment of a vacancy is biased towards particular
 109 elements using nomenclature from Li *et al.* [33]. For example, for a vacancy in a body-centred cubic
 110 lattice surrounded by 8 atoms of elements A, B, C, D and E, a measure of (2,2,2,1,1), respectively would
 111 indicate a relatively unbiased vacancy without predilection for any particular element. A measure of
 112 (5,3,0,0,0) indicates a biased local arrangement, and a measure of (8,0,0,0,0) indicates that all local
 113 atoms within an appropriate cut off distance are of a single element, A. From this notation, we
 114 calculate an overall measure of local element bias per vacancy via

$$115 \quad \text{local element bias} = \sqrt{\frac{1}{N} \sum_{i=\text{element } A}^E (j_i - nx_i)^2} \quad (1)$$

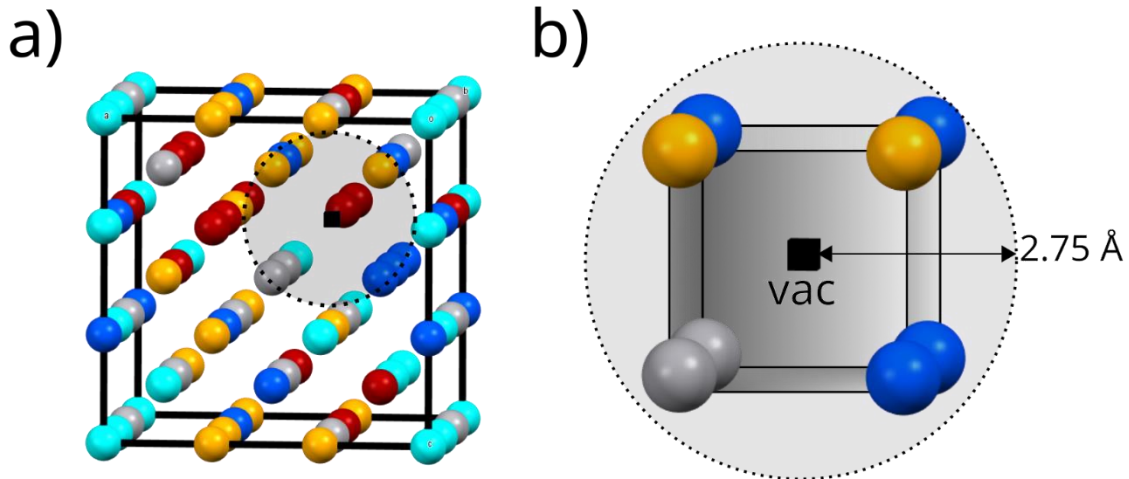
116 Where N is the total number of elements in the alloy, n is the coordination number (8 for body-centred
 117 cubic, 12 for face-centred cubic and hexagonal close-packed), x_j is the atomic fraction of element j , j
 118 is the number atoms of each element, A to E, surrounding a vacancy, and \bar{j} is the mean number of
 119 atoms of each elements surrounding vacancies in an infinitely random solid solution (calculated to be
 120 1.6 for an equiatomic quinary body-centred cubic alloy). and **equation 1** resembles that of the root-
 121 mean-square deviation. For the previous examples, (2,2,2,1,1), (5,3,0,0,0), and (8,0,0,0,0), we
 122 respectively obtain local element biases of 1.04, 3.46, and 4.29, with more examples listed in
 123 **Supplementary Table S1**. Each alloy is assumed to be completely equiatomic among constituent
 124 elements in **equation 1** and has negligible effect on the biases calculated (**Supplementary Figure S3**).

125

126 *2.4. Calculating vacancy volumes*

127 Vacancy volume is calculated by calculating the volume of the convex hull constructed between
 128 coordinates of the nearest neighbour atoms to the vacancy chosen with a cut off distance of 2.75 Å to
 129 include first nearest neighbours but exclude second and further nearest neighbours. **Figure 1a**
 130 illustrates a body-centred cubic 53-atom cell with a vacancy. **Figure 1b** indicates the cut off radius
 131 around the vacancy used to calculate the vacancy volume. However, in some alloys with large lattice
 132 strain some 9 or so neighbours can exist within the cut off distance. Due to the small number of these
 133 occurrences, we therefore treat all these atoms as 1st nearest neighbours similar to previous work [27]
 134 for calculations involving local bias or vacancy volume.

135



136

137 **Figure 1. Vacancy volume of body-centred cubic supercells.** a) vacancy within a body-centred cubic
 138 supercell, and b) atoms within the cut off radius used to calculate vacancy volume.

139

140 2.5. Vacancy formation energy calculations

141 Vacancy formation enthalpies were calculated by structurally relaxing each 54-atom supercell at
 142 constant pressure. Each atom was then removed in turn, and the supercell allowed to relax around
 143 the vacancy, again, at constant pressure. The vacancy formation enthalpy, H_f^V , is calculated via

$$144 H_f^V = E_v - E_0 + \mu_v \quad (2)$$

145 where E_v is the total energy of the supercell containing a vacancy, E_0 is the total energy of the
 146 supercell without a vacancy, and μ_v is the chemical potential of the removed species. The sign of μ_v
 147 corresponds to either a vacancy (+ sign) or an interstitial (- sign). In the literature, variation of μ_v in
 148 bulk metals versus in complex alloys were found to be insignificant [25,35,39]. For example, Roy et al.
 149 investigated the relationship between μ_v in the refractory Mo-Ta-Ti-W-Zr system and their constituent
 150 pure metals and found that the chemical potential differed by less than 1.1% [35]. Herein, we
 151 approximate the chemical potential of the defect species as that in its bulk metal form via the equation

$$152 H_f^V = E_v - E_0 + E_{\text{defect}} \quad (3)$$

153 where E_{defect} is the total energy, normalised to energy-per-atom, of the pure metal in its bulk form at
 154 0 K (hexagonal close packed Hf, Ti, and Zr, and body-centred cubic Mo, Nb, Ta, and W). The accuracy
 155 of these pure bulk metal lattice energy calculations was similar to that of the alloy supercells.

156

157 2.6. General calculation information

158 Each supercell afforded 54 unique vacancy formation enthalpies. These were calculated at least in
 159 duplicate for each quinary alloy in the Hf-Mo-Nb-Ta-Ti-W-Zr system (using a different special quasi-
 160 random structure supercell each time), yielding a total of at least 108 vacancy formation enthalpies
 161 per alloy. The element whose number of atoms is slightly deficient in each supercell, was allowed to
 162 vary at random, and no significant effect of this was observed in the resulting distributions of vacancy

163 formation enthalpies (via a two-tailed Kolmogorov-Smirnov test). Datasets and calculation outputs
 164 will be made available on request to the author.

165 To interrogate any correlations between vacancy formation enthalpy and bulk properties, such that
 166 H_f^V might be predicted using easily obtained properties, the Pearson product-moment correlation
 167 coefficient between H_f^V and several properties were calculated including electron valence
 168 concentration, atomic size mismatch factor, and lattice parameter. These properties are easily
 169 obtained via the parametric approach to phase stability of concentrated solid solution alloys [49–51].

170

171 3. Results and discussion

172 3.1. Phase stability and structure

173 Before assessment of vacancies, the stability and properties of the perfect solid solutions are
 174 investigated. The various properties will be subsequently used to assess the impact on vacancy
 175 formation enthalpies. The solid solution formability of high entropy alloys has been estimated via
 176 various parametric approaches in the past [52–54]. We calculate the solid solution mixing enthalpy,
 177 ΔH_{mix} , for equiatomic alloys via the regular solid solution model given by Yang *et al.* [54], ideal
 178 configurational entropy, ΔS_{conf} , valence electron concentration [53], (VEC), atomic size mismatch
 179 parameter, δ , solid solution formability parameter at the theoretical melting point [54], Ω , and the
 180 atomic packing parameter, γ [55].

181

$$182 \quad \Delta H_{\text{mix}} = \sum_{i=1, i \neq j}^n 4\Delta H_{ij}^{\text{mix}} c_i c_j \quad (4)$$

$$183 \quad \Delta S_{\text{conf}} = -R \sum_{i=1}^n (c_i \ln(C_i)) \quad (5)$$

$$184 \quad \text{VEC} = \sum_{i=1}^n c_i (\text{VEC})_i \quad (6)$$

$$185 \quad \delta = 100 \times \sqrt{\sum_{i=1}^n c_i \left(1 - \frac{r_i}{\bar{r}}\right)^2} \quad (7)$$

$$186 \quad \Omega = \frac{T_m \Delta S_{\text{mix}}}{|\Delta H_{\text{mix}}|}; T_m = \sum_{i=1}^n c_i (T_m)_i \quad (8)$$

$$187 \quad \omega_s = 1 - \sqrt{\frac{(r_L + \bar{r})^2 - \bar{r}^2}{(r_L + \bar{r})^2}}; \omega_L = 1 - \sqrt{\frac{(r_s + \bar{r})^2 - \bar{r}^2}{(r_s + \bar{r})^2}}; \gamma = \frac{\omega_s}{\omega_L} \quad (9)$$

188 Where c_i and c_j are the atomic fractions of elements i and j , respectively. $\Delta H_{ij}^{\text{mix}}$ is the enthalpy of
 189 mixing of binary liquid alloys, based on the Miedema macroscopic model for liquid binary alloys
 190 obtained from Takeuchi *et al.* [56]. R is the ideal gas constant in $\text{JK}^{-1}\text{mol}^{-1}$, $(\text{VEC})_i$ is the valence
 191 electron concentration of the i^{th} element, $\bar{r} = \sum_{i=1}^n c_i r_i$ is the average atomic radius and r_i is the atomic
 192 radius of element i , $(T_m)_i$ is the melting point of the i^{th} element.

193 The putative boundaries for each parameter for solid-solution formation are: $-15 \text{ kJmol}^{-1} <$
 194 $\Delta H_{\text{mix}} < 5 \text{ kJmol}^{-1}$ [52]; $12 \text{ JK}^{-1}\text{mol}^{-1} < \Delta S_{\text{mix}} < 17.5 \text{ JK}^{-1}\text{mol}^{-1}$ [52,54]; $\text{VEC} \leq 6.87$ for body-
 195 centred cubic structures, $\text{VEC} \geq 8$ for face-centred cubic structures [53]; $\delta \leq 6.6\%$ [52]; $\Omega \geq 1.1$ [54];
 196 and $\gamma \leq 1.175$ [55]. The calculated values for the thermophysical parameters in the present alloys are
 197 in **Table 1**.

198

199 **Table 1. Thermophysical parameters for equiatomic alloys. ΔH_{mix} , δ , VEC, γ , and Ω .**

composition	ΔH_{mix} (kJmol ⁻¹)	δ (%)	VEC	γ	Ω
HfMoNbTaTi	-1.44	6.23	4.8	1.0526	24.87
HfMoNbTaW	-4.64	3.51	5.2	1.0717	8.73
HfMoNbTaZr	-1.12	3.56	4.8	1.0341	32.42
HfMoNbTiW	-4.48	6.06	5	1.0719	8.24
HfMoNbTiZr	-1.6	6.68	4.6	1.0523	20.44
HfMoNbWZr	-4.96	3.94	5	1.0712	7.54
HfMoTaTiW	-4.48	6.18	5	1.0719	8.56
HfMoTaTiZr	-1.92	6.73	4.6	1.0523	17.79
HfMoTaWZr	-4.96	3.94	5	1.0712	7.83
HfMoTiWZr	-5.6	6.7	4.8	1.0714	6.29
HfNbTaTiW	-2.72	6.11	4.8	1.0719	13.95
HfNbTaTiZr	2.72	6.46	4.4	1.0523	12.41
HfNbTaWZr	-2.56	3.03	4.8	1.0712	15.02
HfNbTiWZr	-3.04	3.03	4.8	1.0714	11.46
HfTaTiWZr	-3.36	3.03	4.8	1.0714	10.8
MoNbTaTiW	-5.28	4.95	5.2	1.0362	7.39
MoNbTaTiZr	-1.76	5.97	4.8	1.0526	19.77
MoNbTaWZr	-5.44	3.16	5.2	1.0717	7.26
MoNbTiWZr	-5.28	5.75	5	1.0719	6.8
MoTaTiWZr	-5.28	5.88	5	1.0719	7.07
NbTaTiWZr	-3.2	5.85	4.8	1.0719	11.54

200

201 All present alloys satisfy the boundaries for solid solution phase formation for ΔH_{mix} , ΔS_{conf} , Ω , and
 202 γ . VEC of the alloys are below 6.87 which suggests a body-centred cubic is preferred [53]. The alloys
 203 HfMoNbTiZr, HfMoTaTiZr, and HfMoTiWZr have δ values of 6.68, 6.73, and 6.7, respectively, which
 204 suggest these alloys may not form solid solutions. HfNbTaTiZr has a positive mixing enthalpy of
 205 $\Delta H_{\text{mix}} = +2.72 \text{ kJmol}^{-1}$ which suggests a miscibility gap at 0 K.

206 The parametric method suggests that the alloys investigated in this paper produce stable body-
 207 centred cubic solutions. However, there is a lack of information regarding the thermal stability of the
 208 alloys that were investigated in this work. It is possible for local ordering, precipitation, segregation,
 209 and clustering of elements to occur, which will influence the vacancy energetics within the alloy.
 210 HfNbTaTiZr, for instance, has a positive ΔH_{mix} , indicating a thermodynamic tendency to decompose
 211 at low temperatures. MoNbTaTiW is known to undergo B2-like ordering at intermediate
 212 temperatures, which may influence the vacancy formation enthalpies of this alloy. Vacancy sinks, such
 213 as grain boundaries, are another factor that has an impact on the vacancy concentrations in

214 concentrated solid solutions. Additionally, vacancy migration contributes to the observed vacancy
215 concentrations in real materials. Migration is affected by dislocation density [57], clustering of
216 vacancies, and the presence of defect sinks like grain boundaries.

217

218 3.2. Calculating lattice constants

219 There is no generally agreed upon method in literature for calculating lattice constants for HEAs or
220 alloys in general. Experimentally, this is normally determined via a technique such as X-ray diffraction
221 where the maximum peak intensity points are used to assess the general structure of the material.
222 Lattice constants for the alloys in this study were predicted via three methods:

- 223 1. The cube root of the total supercell volume is taken and divided by the unit cell width (3 for
224 a $3 \times 3 \times 3$ cubic supercell) and this is taken as an estimate for the lattice constant across the
225 cell.
- 226 2. All neighbour distances across the cell are measured and the mean of those expected around
227 the 2nd nearest neighbour (similar treatment to Wang *et al.* [27]) are taken to be
228 representative of the alloy.
- 229 3. The rule of mixtures (Vegard's law [58]) is applied to lattice constants of fully relaxed body-
230 centred cubic supercells of pure elements in the Hf-Mo-Nb-Ta-Ti-W-Zr system. This third
231 method is known to neglect the influence of lattice distortion on the crystal and is therefore
232 likely to overpredict lattice parameter of concentrated solid solution alloys.

233 A discussion of methods to calculate the lattice constant in high entropy alloy supercells is found in
234 **Supplementary Figure S4**. It was found that by cube rooting the volume and dividing by the unit cell
235 width (Method 1), was able to provide an average lattice constant whilst taking into account the
236 distortion of the lattice. The lattice constant of the present alloys is in **Table 2**. The volume averaging
237 scheme was used for subsequent correlation studies.

238

239 **Table 2. Lattice constant of refractory alloys calculated via the volume averaging scheme.**

composition	lattice constant (Å)
HfMoNbTaTi	3.31 ± 0.01
HfMoNbTaW	3.29 ± 0.01
HfMoNbTaZr	3.38 ± 0.01
HfMoNbTiW	3.28 ± 0.01
HfMoNbTiZr	3.36 ± 0.01
HfMoNbWZr	3.34 ± 0.01
HfMoTaTiW	3.28 ± 0.01
HfMoTaTiZr	3.37 ± 0.01
HfMoTaWZr	3.35 ± 0.01
HfMoTiWZr	3.34 ± 0.01
HfNbTaTiW	3.32 ± 0.01
HfNbTaTiZr	3.41 ± 0.01
HfNbTaWZr	3.38 ± 0.01
HfNbTiWZr	3.38 ± 0.01

HfTaTiWZr	3.37 ± 0.01
MoNbTaTiW	3.23 ± 0.01
MoNbTaTiZr	3.32 ± 0.01
MoNbTaWZr	3.30 ± 0.01
MoNbTiWZr	3.28 ± 0.01
MoTaTiWZr	3.29 ± 0.01
NbTaTiWZr	3.32 ± 0.01

240

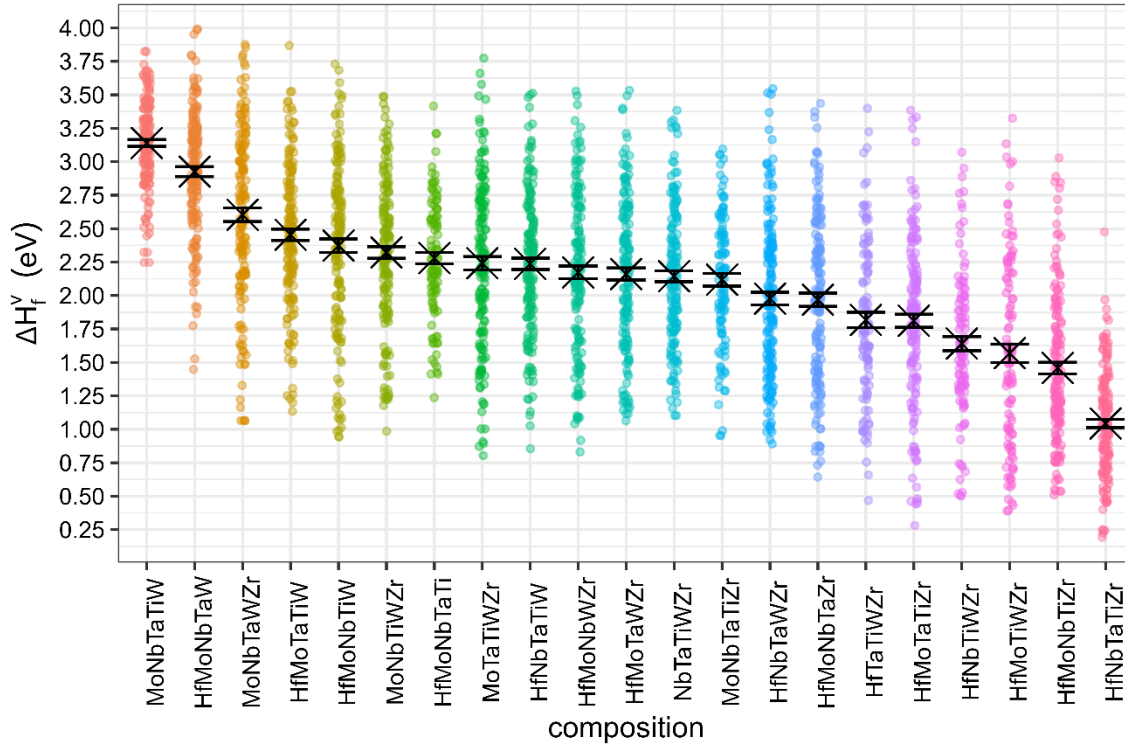
241 3.3. Vacancy formation enthalpies

242 At least 2 unique special quasi-random cells were generated for each of the 21 alloys in the study. To
 243 determine if each special quasi-random cell produced enthalpies likely from the same population
 244 distribution, we performed a two-tailed Kolmogorov-Smirnov test between each sample distribution
 245 (**Supplementary Table S2**). After confirming we likely adequately sampled the same probability
 246 distribution for each alloy, we combined each sample distribution to produce a single distribution of
 247 energies for each alloy. For completeness, the vacancy formation enthalpies for the pure hexagonal
 248 close packed (Hf: 2.20; Ti: 2.04; and Zr: 1.98 eV) and body-centred cubic (Mo: 2.80; Nb: 2.62; Ta: 2.83;
 249 and W: 3.33 eV) elements were calculated.

250

251 The vacancy formation enthalpy adopts a single value in pure elements. However, the local chemical
 252 variations in concentrated solid solutions produce a distribution of vacancy formation enthalpies. The
 253 calculated enthalpies of the quinary Hf-Mo-Nb-Ta-Ti-W-Zr alloys are in **Figure 2** (ordered from highest
 254 to lowest mean values for H_f^V) The largest mean H_f^V belongs to MoNbTaTiW, which, incidentally, is the
 255 most reported quinary refractory alloy in literature [59–62]. The mean H_f^V for MoNbTaTiW is 3.14 eV
 256 and is similar to body-centred cubic W (3.11 [63] – 3.19 [64] via density functional theory, and 3.1 -
 257 3.4 eV experimentally [65]). HfNbTaTiZr exhibited the lowest mean enthalpy of vacancy formation of
 258 1.04 eV which is similar to low melting face-centred cubic elements like Cu (1.33 eV) and Ag (0.96 eV)
 259 [66]. This indicates the possible low thermal stability of these solid solutions, and the high probability
 260 that these alloys either have a low relative melting point compared to alloys in this study, or that they
 261 decompose into more stable, multiphase systems The rest of the solid solutions considered in this
 262 study exhibited intermediate H_f^V , with mean values from 1.46 – 2.93 eV. Mean values of H_f^V for all
 263 alloys in this study are in **Table 3**.

264



265

266

267 **Figure 2. Vacancy formation enthalpy for equiatomic alloys in the Hf-Mo-Nb-Ta-Ti-W-Zr system.**
 268 H_f^v values are ordered from highest to lowest. A cross indicates mean H_f^v values for each alloy. Error
 269 bars indicate standard error of the mean.

270

271 **Table 3. Mean H_f^v values for concentrated solid solutions.** Where σ is the standard deviation of the
 272 mean H_f^v .

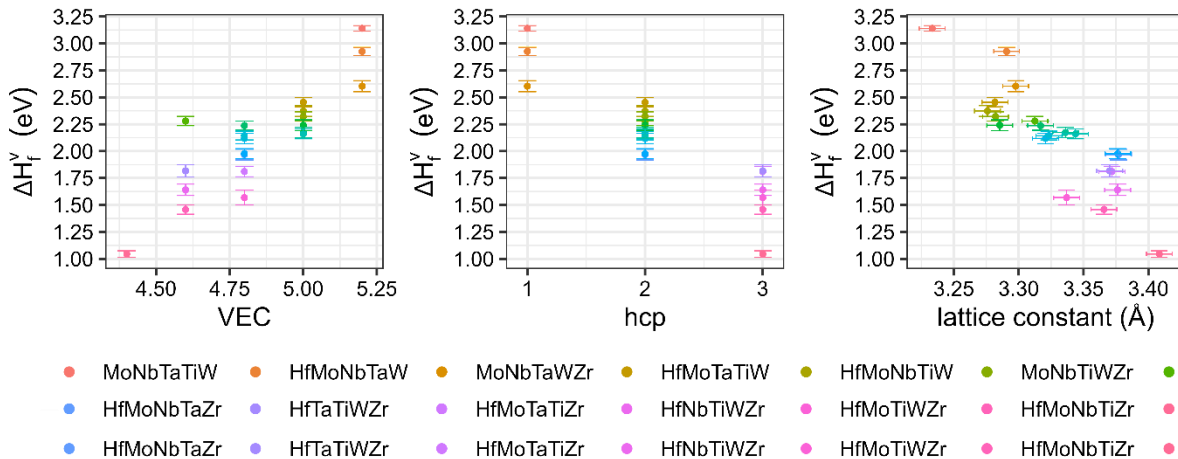
composition	mean H_f^v (eV)	σ (eV)
MoNbTaTiW	3.14	0.32
HfMoNbTaW	2.93	0.48
MoNbTaWZr	2.6	0.65
HfMoTaTiW	2.45	0.54
HfMoNbTiW	2.37	0.64
MoNbTiWZr	2.32	0.56
HfMoNbTaTi	2.28	0.44
HfNbTaTiW	2.24	0.54
MoTaTiWZr	2.24	0.63
HfMoNbWZr	2.17	0.6
HfMoTaWZr	2.16	0.57
NbTaTiWZr	2.14	0.52
MoNbTaTiZr	2.12	0.5
HfNbTaWZr	1.98	0.6
HfMoNbTaZr	1.97	0.63

HfTaTiWZr	1.82	0.61
HfMoTaTiZr	1.81	0.62
HfNbTiWZr	1.64	0.55
HfMoTiWZr	1.57	0.72
HfMoNbTiZr	1.46	0.55
HfNbTaTiZr	1.04	0.39

273

274 There is little correlation between H_f^V and the element being removed [27]. However, H_f^V does depend
 275 on the elements which make up the nearest neighbour environment. For example, Hf, Ti, and Zr have
 276 vacancy formation enthalpies of 2.20, 1.98, and 2.04 eV, respectively. When these elements form the
 277 nearest neighbour environment, H_f^V is likely to decrease. In contrast, the presence of Mo and W as
 278 neighbouring elements (with H_f^V values of 2.80 and 3.33 eV, respectively), is likely to increase H_f^V .
 279 Therefore, the resulting vacancy formation energy appears to be the result of an averaging scheme
 280 based on the local environment. **Supplementary Figure S5** shows the product-moment correlation
 281 coefficients of nearest neighbour elements versus the calculated H_f^V for each environment. Local
 282 element bias was found to have no direct correlation with H_f^V , as a strong bias toward a particular
 283 element shifts the enthalpy of vacancy formation towards that of the biased element.

284 Local properties surrounding each vacancy were collected (vacancy volume, immediate neighbour
 285 atoms) as well as bulk properties of the alloys (valence electron concentration, lattice constant,
 286 average electron shell number, atomic size mismatch factor, δ , among others). The thermophysical
 287 parameters are found in **Table 1**. **Figure 3** shows that the mean H_f^V of the studied alloys strongly
 288 correlates with valence electron concentration (**Figure 3a**: $r = 0.88$), number of hexagonal close
 289 packed alloying elements (**Figure 3b**: $r = -0.91$), and lattice constant (**Figure 3c**: $r = -0.87$). Vacancy
 290 volume, calculated from the convex hull between atomic coordinates of atoms within 2.75 Å around
 291 the removed atom, was found to weakly correlate with H_f^V ($r = +0.28$; **Supplementary Figure S6**).



292

293 **Figure 3. Mean H_f^V values for alloys in the Hf-Mo-Nb-Ta-Ti-W-Zr system plotted versus a) valence**
 294 **electron concentration; b) number of constituent hexagonal close packed elements; and c) calculated**
 295 **lattice constant. Vertical error bars indicate the standard error of the mean of H_f^V ; horizontal error**
 296 **bars indicate maximum deviation observed in lattice parameter across all the alloys.**

297

3298 H_f^V is largely dependent on the first nearest neighbours [67]. This suggests that element clustering and
 3299 segregation have a significant role in defining the vacancy energies of real materials. In addition, the
 3300 enthalpies at the lower end of the distribution have a greater impact on the equilibrium vacancy
 3301 concentration. Future research should make a concerted effort to sample these smaller enthalpies.
 3302 The enthalpy of vacancy formation has been found to correspond with bulk parameters such as lattice
 3303 constant, valence electron concentration, and several Hume-Rothery factors including the preferred
 3304 crystal structure of the constituent elements at 0 K. These parameters may be used as a simple
 3305 empirical relation to estimate H_f^V as a first approximation.

3306

3307 3.4. Population of vacancies in Hf-Mo-Nb-Ta-Ti-W-Zr quinary alloys

3308 The value of H_f^V can be used to estimate probability of vacancy formation and therefore the vacancy
 3309 concentration, X_i , in a material [68]. Similar to Daigle *et al.*, we calculate the vacancy concentration in
 3310 equiatomic concentrated solid solutions with the configurational entropy of the added monovacancy
 3311 (**equation 10**) [20]. Furthermore, we compute the vacancy concentration using the entire enthalpy
 3312 distribution, which takes into account the preferential formation of vacancies with enthalpies at the
 3313 lower tail of the H_f^V distribution (**equation 11**).

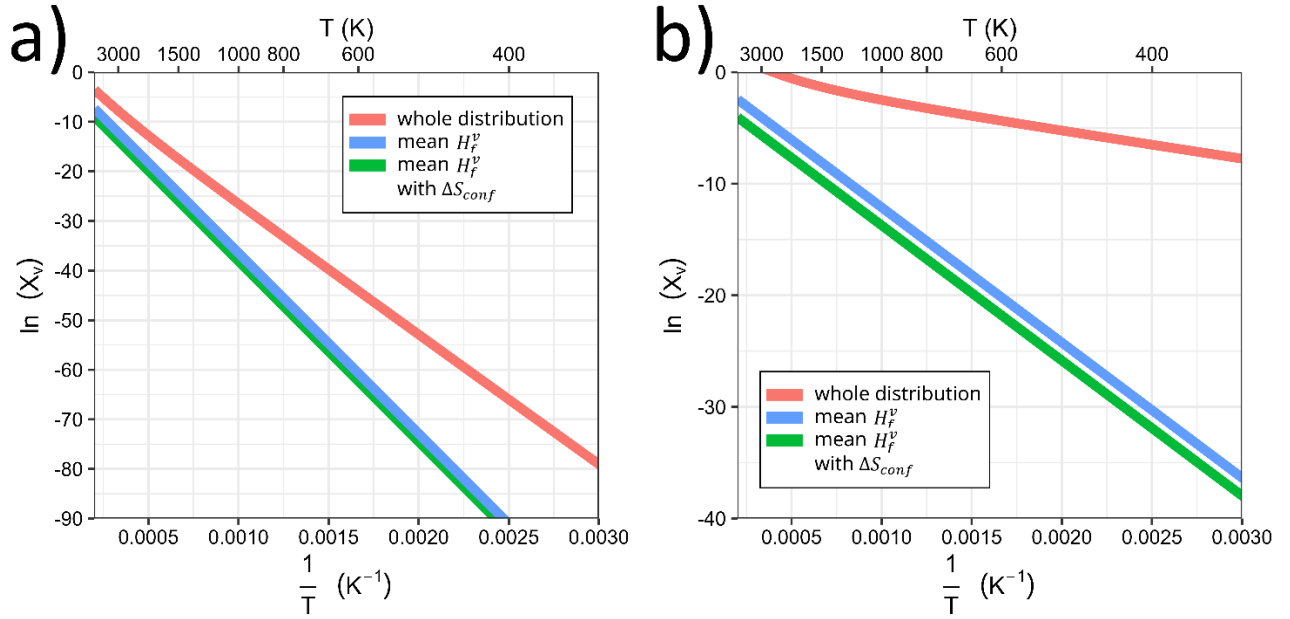
$$3314 \quad X_i = \frac{n}{N} = \frac{1}{m} e^{\frac{-\Delta H_f^V}{k_B T}} \quad (10)$$

$$3315 \quad X_i = \frac{n}{N} = \frac{\sum_{i=1}^n \frac{1}{m} e^{\frac{-\Delta H_f^V(i)}{k_B T}}}{n} \quad (11)$$

3316 where $\frac{n}{N}$ is the fraction of vacancies in the system, m is the alloying number, ΔH_f^V is the mean enthalpy
 3317 of monovacancy formation (eV), k_B is the Boltzmann constant (eVK⁻¹), T is temperature (K), $\Delta H_f^V(i)$ is
 3318 the enthalpy of vacancy formation for the i^{th} observation, and n is the number of observations.
 3319 **Equation 10** considers the configurational entropy of adding a vacancy to an m number of elements
 3320 at the dilute limit and is with accordance to the $m + 1$ species scheme [69]. Adding a vacancy to
 3321 concentrated solid solutions results in a lower additional configurational entropy with increasing m
 3322 (**Supplementary Figure S7**). The derivation for **equation 10** is given in **Supplementary Appendix 1**.

3323 We calculate the equilibrium vacancy concentration here for two alloys, MoNbTaTiW, and HfNbTaTiZr,
 3324 using a) the mean H_f^V only; b) with the additional configurational entropy of the vacancy; and c) by
 3325 using the entire distribution of H_f^V . From **Figure 4a**, the configurational entropy associated with
 3326 monovacancies in complex materials reduces their concentration in the MoNbTaTiW alloy compared
 3327 with pure metals and dilute alloys. However, when the entire distribution of energies is considered,
 3328 there is a significantly higher concentration of vacancies throughout the entire temperature range.
 3329 This is because vacancies with lower formation enthalpies preferentially form within the alloy crystal,
 3330 and therefore contribute most to the equilibrium vacancy concentration. Likewise, the same effect
 3331 can be seen in **Figure 4b** for HfNbTaTiZr. In both cases, the equilibrium vacancy concentration
 3332 significantly deviates from typical Arrhenius behaviour especially at temperatures > 2000 K. This
 3333 non-Arrhenius dependence of vacancy concentration is found to be characteristic for all HEAs in the
 3334 present study (**Supplementary Figure S8**) and may be a general property of all high entropy systems
 3335 such as high entropy alloys and high entropy ceramics.

3336



337

338 **Figure 4. Equilibrium vacancy concentration versus temperature.** For a) MoNbTaTiW; and b)
 339 HfNbTaTiZr. X_v is the equilibrium vacancy concentration, $X_v = \frac{n}{N}$.

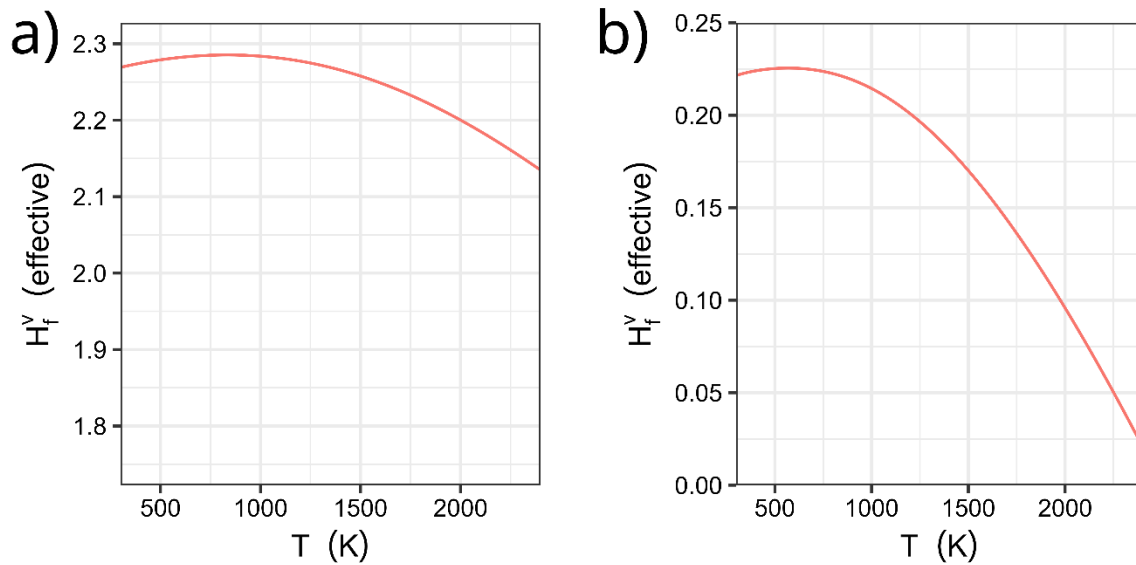
340

341 By considering the entire distribution of monovacancy formation in HEAs, it is possible to compute an
 342 effective H_f^v as if the solid solution were a pure element. For the alloys in this study, this result is
 343 significantly lower than the mean H_f^v that is typically used previously to predict vacancies in pure
 344 elements and dilute alloys:

$$345 \quad H_f^v(\text{effective}) = -k_B T \ln \left(\frac{\sum_{i=1}^n \frac{1}{m} e^{\frac{-\Delta H_f^v(i)}{k_B T}}}{n} \right) \quad (12)$$

346 where $\Delta H_f^v(i)$ is the enthalpy of vacancy formation for the i^{th} observation, and n is the number of
 347 observations. We compute the effective H_f^v for MoNbTaTiW and HfNbTaTiZr using **equation 12**. **Figure**
 348 **5a** depicts the temperature dependence of the effective H_f^v for MoNbTaTiW. An effective H_f^v below
 349 3.14 eV for MoNbTaTiW implies that monovacancies form much more easily at lower temperatures
 350 than if a simple average H_f^v is used. Similarly, **Figure 5b** illustrates effective H_f^v for HfNbTaTiZr. In both
 351 cases, the effective H_f^v is significantly lower than the mean H_f^v (MoNbTaTiW: 3.14 eV; HfNbTaTiZr:
 352 1.04 eV).

353



354

355 **Figure 5. Effective H_f^v versus temperature.** For a) MoNbTaTiW; and b) HfNbTaTiZr.

356 Our findings indicate that the higher equilibrium concentration of monovacancies observed
 357 experimentally in HEAs is primarily driven by the spread of vacancy formation enthalpies (H_f^v) inherent
 358 in these materials. Specifically, the deviation of the effective H_f^v from the mean H_f^v increases with the
 359 spread of H_f^v values (for example, shown in **Figure 2**), resulting in more vacancies than those predicted
 360 for simple pure metals and conventional alloys.

361

362 **Summary**

363 In this work, we examine the vacancy formation enthalpies and associated equilibrium vacancy
 364 concentrations of quinary alloys in the Hf-Mo-Nb-Ta-Ti-W-Zr system using density functional theory
 365 calculations. It is shown that while configurational entropy reduces vacancy concentration in these
 366 multicomponent systems, the lower tails in the enthalpy distribution caused by complex local
 367 environments around each vacancy lead to superabundant vacancies. This mechanism is likely to be
 368 active in both ordinary alloys and compositionally complex materials. This work provides insight into
 369 vacancy formation and equilibrium vacancy concentrations of high entropy alloys. Future analyses will
 370 investigate local ordering of elements and its effect on vacancy concentration.

371

372 **Declaration of Competing Interest**

373 The authors declare that they have no known competing financial interests or personal relationships
 374 that could have appeared to influence the work reported in this paper.

375

376 **Acknowledgements**

377 JAW is funded through the Nuclear Energy Futures Centre for Doctoral Training (EP/S023844/1), co-
 378 sponsored by the National Nuclear Laboratory (NNL). SCM is funded through the Sêr Cymru II
 379 programme by Welsh European Funding Office (WEFO) under the European Regional Development
 380 Fund (ERDF). CM is funded through the Knowledge Economy Skills Scholarships (KESS 2) programme

381 which is part funded through the Welsh government's European Social Fund (ESF). Computing
382 resources were made available by Supercomputing Wales operated by Cardiff University
383 (www.supercomputing.wales) and by the Cambridge Service for Data Driven Discovery (CSD3)
384 operated by the University of Cambridge Research Computing Service (www.csd3.cam.ac.uk).

385

386 References

- 387 [1] B. Cantor, I.T.H. Chang, P. Knight, A.J.B. Vincent, Microstructural development in equiatomic
388 multicomponent alloys, *Mater. Sci. Eng. A.* 375–377 (2004) 213–218.
389 <https://doi.org/10.1016/j.msea.2003.10.257>.
- 390 [2] J.W. Yeh, S.K. Chen, S.J. Lin, J.Y. Gan, T.S. Chin, T.T. Shun, C.H. Tsau, S.Y. Chang,
391 Nanostructured high-entropy alloys with multiple principal elements: Novel alloy design
392 concepts and outcomes, *Adv. Eng. Mater.* 6 (2004) 299-303+274.
393 <https://doi.org/10.1002/adem.200300567>.
- 394 [3] J. Wilson, L. Evitts, M. Rushton, D. Goddard, S. Middleburgh, W. Lee, High entropy alloys for
395 accident tolerant fuel applications, in: *TopFuel, TopFuel 2021*, 2021.
396 https://www.researchgate.net/publication/361225055_High_entropy_alloys_for_accident_tolerant_fuel_applications (accessed July 19, 2022).
- 398 [4] E.J. Pickering, A.W. Carruthers, P.J. Barron, S.C. Middleburgh, D.E.J. Armstrong, A.S. Gandy,
399 High-entropy alloys for advanced nuclear applications, *Entropy.* 23 (2021) 1–28.
400 <https://doi.org/10.3390/e23010098>.
- 401 [5] M. Dada, P. Popoola, S. Adeosun, N. Mathe, M. Dada, P. Popoola, S. Adeosun, N. Mathe, High
402 Entropy Alloys for Aerospace Applications, *IntechOpen*, n.d. www.intechopen.com (accessed
403 June 7, 2021).
- 404 [6] M.H. Tsai, J.W. Yeh, High-entropy alloys: A critical review, *Mater. Res. Lett.* 2 (2014) 107–123.
405 <https://doi.org/10.1080/21663831.2014.912690>.
- 406 [7] Y.J. Zhou, Y. Zhang, Y.L. Wang, G.L. Chen, Solid solution alloys of AlCoCrFeNi Tix with excellent
407 room-temperature mechanical properties, *Appl. Phys. Lett.* 90 (2007) 181904.
408 <https://doi.org/10.1063/1.2734517>.
- 409 [8] F. Müller, B. Gorr, H.-J.J. Christ, J. Müller, B. Butz, H. Chen, A. Kauffmann, M. Heilmaier, On
410 the oxidation mechanism of refractory high entropy alloys, *Corros. Sci.* 159 (2019) 108161.
411 <https://doi.org/10.1016/j.corsci.2019.108161>.
- 412 [9] F. Müller, B. Gorr, H.J. Christ, H. Chen, A. Kauffmann, M. Heilmaier, Effect of Y Additions on
413 the Oxidation Behaviour of Novel Refractory High-Entropy Alloy NbMoCrTiAl at 1000 °C in Air,
414 *Oxid. Met.* 94 (2020) 147–163. <https://doi.org/10.1007/S11085-020-09983-6/FIGURES/10>.
- 415 [10] T.M. Butler, M.L. Weaver, Oxidation behavior of arc melted AlCoCrFeNi multi-component
416 high-entropy alloys, *J. Alloys Compd.* 674 (2016) 229–244.
417 <https://doi.org/10.1016/j.jallcom.2016.02.257>.
- 418 [11] T.M. Butler, K.J. Chaput, J.R. Dietrich, O.N. Senkov, High temperature oxidation behaviors of
419 equimolar NbTiZrV and NbTiZrCr refractory complex concentrated alloys (RCCAs), *J. Alloys
420 Compd.* 729 (2017) 1004–1019. <https://doi.org/10.1016/J.JALLCOM.2017.09.164>.
- 421 [12] Z.D. Han, H.W. Luan, X. Liu, N. Chen, X.Y. Li, Y. Shao, K.F. Yao, Microstructures and mechanical
422 properties of TixNbMoTaW refractory high-entropy alloys, *Mater. Sci. Eng. A.* 712 (2018) 380–
423 385. <https://doi.org/10.1016/j.msea.2017.12.004>.

- 424 [13] B. Christiaen, C. Domain, L. Thuinet, A. Ambard, A. Legris, Influence of vacancy diffusional
425 anisotropy: Understanding the growth of zirconium alloys under irradiation and their
426 microstructure evolution, *Acta Mater.* 195 (2020) 631–644.
427 <https://doi.org/10.1016/J.ACTAMAT.2020.06.004>.
- 428 [14] W. Sun, Y. Zhu, R. Marceau, L. Wang, Q. Zhang, X. Gao, C. Hutchinson, Precipitation
429 strengthening of aluminum alloys by room-temperature cyclic plasticity, *Science (80-.)*. 363
430 (2019) 972–975.
431 https://doi.org/10.1126/SCIENCE.AAV7086/SUPPL_FILE/AAV7086_SUN_SM.PDF.
- 432 [15] M.H. Cui, T.L. Shen, H.P. Zhu, J. Wang, X.Z. Cao, P. Zhang, L.L. Pang, C.F. Yao, K.F. Wei, Y.B.
433 Zhu, B.S. Li, J.R. Sun, N. Gao, X. Gao, H.P. Zhang, Y.B. Sheng, H.L. Chang, W.H. He, Z.G. Wang,
434 Vacancy like defects and hardening of tungsten under irradiation with He ions at 800 °C,
435 *Fusion Eng. Des.* 121 (2017) 313–318. <https://doi.org/10.1016/J.FUSENGDES.2017.05.043>.
- 436 [16] Q. Xu, H.Q. Guan, Z.H. Zhong, S.S. Huang, J.J. Zhao, Irradiation resistance mechanism of the
437 CoCrFeMnNi equiatomic high-entropy alloy, *Sci. Reports* 2021 111. 11 (2021) 1–8.
438 <https://doi.org/10.1038/s41598-020-79775-0>.
- 439 [17] F. Ruicheng, C. Hui, L. Haiyan, R. Zhiyuan, Y. Changfeng, Effects of Vacancy Concentration and
440 Temperature on Mechanical Properties of Single-Crystal γ -TiAl Based on Molecular Dynamics
441 Simulation, *High Temp. Mater. Process.* 37 (2018) 113–120. [https://doi.org/10.1515/HTMP-
442 2016-0156/MACHINEREADEABLECITATION/RIS](https://doi.org/10.1515/HTMP-2016-0156/MACHINEREADEABLECITATION/RIS).
- 443 [18] J. Peng, B. Xie, X. Zeng, Q. Fang, B. Liu, P.K. Liaw, J. Li, Vacancy dependent mechanical
444 behaviors of high-entropy alloy, *Int. J. Mech. Sci.* 218 (2022) 107065.
445 <https://doi.org/10.1016/J.IJMECSCI.2022.107065>.
- 446 [19] Z. Wang, C.T. Liu, P. Dou, Thermodynamics of vacancies and clusters in high-entropy alloys,
447 *Phys. Rev. Mater.* 1 (2017) 043601.
448 <https://journals.aps.org/prmaterials/abstract/10.1103/PhysRevMaterials.1.043601> (accessed
449 September 11, 2021).
- 450 [20] S.E. Daigle, D.W. Brenner, Statistical approach to obtaining vacancy formation energies in
451 high-entropy crystals from first principles calculations: Application to a high-entropy diboride,
452 *Phys. Rev. Mater.* 4 (2020) 123602.
453 <https://doi.org/10.1103/PHYSREVMATERIALS.4.123602/FIGURES/6/MEDIUM>.
- 454 [21] D.E. Jodi, T.A. Listyawan, P. Hruska, J. Cizek, N. Park, U. Lee, Study of vacancies in
455 $\text{Fe}_{x}(\text{CoCrMnNi})_{100-x}$ medium- and high-entropy alloys by positron annihilation spectroscopy,
456 *Scr. Mater.* 194 (2021) 113654. <https://doi.org/10.1016/J.SCRIPTAMAT.2020.113654>.
- 457 [22] K. Sugita, N. Matsuoka, M. Mizuno, H. Araki, Vacancy formation enthalpy in CoCrFeMnNi
458 high-entropy alloy, *Scr. Mater.* 176 (2020) 32–35.
459 <https://doi.org/10.1016/J.SCRIPTAMAT.2019.09.033>.
- 460 [23] M. Vaidya, K.G. Pradeep, B.S. Murty, G. Wilde, S. V. Divinski, Bulk tracer diffusion in CoCrFeNi
461 and CoCrFeMnNi high entropy alloys, *Acta Mater.* 146 (2018) 211–224.
462 <https://doi.org/10.1016/J.ACTAMAT.2017.12.052>.
- 463 [24] X. Zhang, S. V. Divinski, B. Grabowski, Ab initio prediction of vacancy energetics in HCP Al-Hf-
464 Sc-Ti-Zr high entropy alloys and the subsystems, *Acta Mater.* (2022) 117677.
465 <https://doi.org/10.1016/J.ACTAMAT.2022.117677>.
- 466 [25] M. Mizuno, K. Sugita, H. Araki, Defect energetics for diffusion in CrMnFeCoNi high-entropy
467 alloy from first-principles calculations, *Comput. Mater. Sci.* 170 (2019) 109163.

- 468 <https://doi.org/10.1016/J.COMMATSCI.2019.109163>.
- 469 [26] D. Vizoso, C. Deo, Determination of Vacancy Formation Energies in Binary UZr Alloys Using
470 Special Quasirandom Structure Methods, *Front. Mater.* 8 (2021) 243.
471 <https://doi.org/10.3389/FMATS.2021.692660/BIBTEX>.
- 472 [27] Y. Wang, X. Li, X. Li, Y. Zhang, Y. Zhang, Y. Xu, Y. Lei, C.S. Liu, X. Wu, Prediction of vacancy
473 formation energies at tungsten grain boundaries from local structure via machine learning
474 method, *J. Nucl. Mater.* 559 (2022) 153412.
475 <https://doi.org/10.1016/J.JNUCMAT.2021.153412>.
- 476 [28] Y.Z. Wang, Y.J. Wang, Disentangling diffusion heterogeneity in high-entropy alloys, *Acta*
477 *Mater.* 224 (2022) 117527. <https://doi.org/10.1016/J.ACTAMAT.2021.117527>.
- 478 [29] Y. Zhang, A. Manzoor, C. Jiang, D. Aidhy, D. Schwen, A statistical approach for atomistic
479 calculations of vacancy formation energy and chemical potentials in concentrated solid-
480 solution alloys, *Comput. Mater. Sci.* 190 (2021) 110308.
481 <https://doi.org/10.1016/J.COMMATSCI.2021.110308>.
- 482 [30] W. Chen, X. Ding, Y. Feng, X. Liu, K. Liu, Z.P. Lu, D. Li, Y. Li, C.T. Liu, X.Q. Chen, Vacancy
483 formation enthalpies of high-entropy FeCoCrNi alloy via first-principles calculations and
484 possible implications to its superior radiation tolerance, *J. Mater. Sci. Technol.* 34 (2018) 355–
485 364. <https://doi.org/10.1016/J.JMST.2017.11.005>.
- 486 [31] S.C. Middleburgh, D.M. King, G.R. Lumpkin, M. Cortie, L. Edwards, Segregation and migration
487 of species in the CrCoFeNi high entropy alloy, *J. Alloys Compd.* 599 (2014) 179–182.
- 488 [32] A. Esfandiarpour, M.N. Nasrabadi, Vacancy formation energy in CuNiCo equimolar alloy and
489 CuNiCoFe high entropy alloy: ab initio based study, *Calphad.* 66 (2019) 101634.
490 <https://doi.org/10.1016/J.CALPHAD.2019.101634>.
- 491 [33] C. Li, J. Yin, K. Odbadrakh, B.C. Sales, S.J. Zinkle, G.M. Stocks, B.D. Wirth, First principle study
492 of magnetism and vacancy energetics in a near equimolar NiFeMnCr high entropy alloy, *J.*
493 *Appl. Phys.* 125 (2019) 155103. <https://doi.org/10.1063/1.5086172>.
- 494 [34] Z.-S. Nong, Z.-H. Gu, Y.-W. Liu, Z.-Y. Wang, J.-C. Zhu, Formation and migration behavior of
495 vacancy in multi-component alloys, *Intermetallics.* 151 (2022) 107724.
496 <https://doi.org/10.1016/J.INTERMET.2022.107724>.
- 497 [35] A. Roy, P. Singh, G. Balasubramanian, D.D. Johnson, Vacancy formation energies and
498 migration barriers in multi-principal element alloys, *Acta Mater.* 226 (2022) 117611.
499 <https://doi.org/10.1016/J.ACTAMAT.2021.117611>.
- 500 [36] P. Singh, S. Gupta, S. Thimmaiah, B. Thoeny, P.K. Ray, A. V. Smirnov, D.D. Johnson, M.J.
501 Kramer, Vacancy-mediated complex phase selection in high entropy alloys, *Acta Mater.* 194
502 (2020) 540–546. <https://doi.org/10.1016/J.ACTAMAT.2020.04.063>.
- 503 [37] A. Cunliffe, J. Plummer, I. Figueroa, I. Todd, Glass formation in a high entropy alloy system by
504 design, *Intermetallics.* 23 (2012) 204–207. <https://doi.org/10.1016/J.INTERMET.2011.12.006>.
- 505 [38] A.X. Lin-Vines, J.A. Wilson, A. Fraile, L.J. Evitts, M.J.D. Rushton, J.O. Astbury, W.E. Lee, S.C.
506 Middleburgh, Defect behaviour in the MoNbTaVW high entropy alloy (HEA), *Results Mater.*
507 15 (2022) 100320. <https://doi.org/10.1016/J.RINMA.2022.100320>.
- 508 [39] S. Zhao, Defect properties in a VTaCrW equiatomic high entropy alloy (HEA) with the body
509 centered cubic (bcc) structure, *J. Mater. Sci. Technol.* 44 (2020) 133–139.
510 <https://doi.org/10.1016/j.jmst.2019.10.025>.

- 511 [40] P. Hohenberg, W. Kohn, Inhomogeneous electron gas, *Phys. Rev.* 136 (1964) B864.
512 <https://doi.org/10.1103/PhysRev.136.B864>.
- 513 [41] W. Kohn, L.J. Sham, Self-consistent equations including exchange and correlation effects,
514 *Phys. Rev.* 140 (1965) A1133. <https://doi.org/10.1103/PhysRev.140.A1133>.
- 515 [42] A. Van De Walle, P. Tiwary, M. De Jong, D.L. Olmsted, M. Asta, A. Dick, D. Shin, Y. Wang, L.Q.
516 Chen, Z.K. Liu, Efficient stochastic generation of special quasirandom structures, *Calphad*
517 *Comput. Coupling Phase Diagrams Thermochem.* 42 (2013) 13–18.
518 <https://doi.org/10.1016/j.calphad.2013.06.006>.
- 519 [43] G. Kresse, Ab initio molecular dynamics for liquid metals, *J. Non. Cryst. Solids.* 192–193 (1995)
520 222–229. [https://doi.org/10.1016/0022-3093\(95\)00355-X](https://doi.org/10.1016/0022-3093(95)00355-X).
- 521 [44] G. Kresse, J. Furthmüller, Efficiency of ab-initio total energy calculations for metals and
522 semiconductors using a plane-wave basis set, *Comput. Mater. Sci.* 6 (1996) 15–50.
523 [https://doi.org/10.1016/0927-0256\(96\)00008-0](https://doi.org/10.1016/0927-0256(96)00008-0).
- 524 [45] P.E. Blöchl, Projector augmented-wave method, *Phys. Rev. B.* 50 (1994) 17953–17979.
525 <https://doi.org/10.1103/PhysRevB.50.17953>.
- 526 [46] G. Kresse, D. Joubert, From ultrasoft pseudopotentials to the projector augmented-wave
527 method, *Phys. Rev. B.* 59 (1999) 1758. <https://doi.org/10.1103/PhysRevB.59.1758>.
- 528 [47] J.P. Perdew, K. Burke, M. Ernzerhof, Generalized gradient approximation made simple, *Phys.*
529 *Rev. Lett.* 77 (1996) 3865–3868. <https://doi.org/10.1103/PhysRevLett.77.3865>.
- 530 [48] M. Methfessel, A.T. Paxton, High-precision sampling for Brillouin-zone integration in metals,
531 *Phys. Rev. B.* 40 (1989) 3616–3621. <https://doi.org/10.1103/PhysRevB.40.3616>.
- 532 [49] D.J.M.M. King, S.C. Middleburgh, A.G. McGregor, M.B. Cortie, Predicting the formation and
533 stability of single phase high-entropy alloys, *Acta Mater.* 104 (2016) 172–179.
534 <https://doi.org/10.1016/j.actamat.2015.11.040>.
- 535 [50] Tazuddin, N.P. Gurao, K. Biswas, In the quest of single phase multi-component multiprincipal
536 high entropy alloys, *J. Alloys Compd.* 697 (2017) 434–442.
537 <https://doi.org/10.1016/J.JALLCOM.2016.11.383>.
- 538 [51] R. Li, L. Xie, W.Y. Wang, P.K. Liaw, Y. Zhang, High-Throughput Calculations for High-Entropy
539 Alloys: A Brief Review, *Front. Mater.* 7 (2020) 290.
540 <https://doi.org/10.3389/FMATS.2020.00290/BIBTEX>.
- 541 [52] Y. Zhang, Y.J. Zhou, J.P. Lin, G.L. Chen, P.K. Liaw, Solid-solution phase formation rules for
542 multi-component alloys, *Adv. Eng. Mater.* 10 (2008) 534–538.
543 <https://doi.org/10.1002/adem.200700240>.
- 544 [53] S. Guo, C. Ng, J. Lu, C.T. Liu, Effect of valence electron concentration on stability of fcc or bcc
545 phase in high entropy alloys, *J. Appl. Phys.* 109 (2011). <https://doi.org/10.1063/1.3587228>.
- 546 [54] X. Yang, Y. Zhang, Prediction of high-entropy stabilized solid-solution in multi-component
547 alloys, *Mater. Chem. Phys.* 132 (2012) 233–238.
548 <https://linkinghub.elsevier.com/retrieve/pii/S0254058411009357> (accessed February 13,
549 2021).
- 550 [55] Z. Wang, Y. Huang, Y. Yang, J. Wang, C.T. Liu, Atomic-size effect and solid solubility of
551 multicomponent alloys, *Scr. Mater.* 94 (2015) 28–31.
552 <https://doi.org/10.1016/j.scriptamat.2014.09.010>.

- 553 [56] A. Takeuchi, A. Inoue, Classification of Bulk Metallic Glasses by Atomic Size Difference, Heat
554 of Mixing and Period of Constituent Elements and Its Application to Characterization of the
555 Main Alloying Element, *Mater. Trans.* 46 (2005) 2817–2829.
556 https://www.jstage.jst.go.jp/article/matertrans/46/12/46_12_2817/_article (accessed April
557 1, 2021).
- 558 [57] M. Glienke, M. Vaidya, K. Gururaj, L. Daum, B. Tas, L. Rogal, K.G. Pradeep, S. V. Divinski, G.
559 Wilde, Grain boundary diffusion in CoCrFeMnNi high entropy alloy: Kinetic hints towards a
560 phase decomposition, *Acta Mater.* 195 (2020) 304–316.
561 <https://doi.org/10.1016/J.ACTAMAT.2020.05.009>.
- 562 [58] A.R. Denton, N.W. Ashcroft, Vegard’s law, *Phys. Rev. A.* 43 (1991) 3161.
563 <https://doi.org/10.1103/PhysRevA.43.3161>.
- 564 [59] Z.D. Han, N. Chen, S.F. Zhao, L.W. Fan, G.N. Yang, Y. Shao, K.F. Yao, Effect of Ti additions on
565 mechanical properties of NbMoTaW and VNbMoTaW refractory high entropy alloys,
566 *Intermetallics.* 84 (2017) 153–157. <https://doi.org/10.1016/j.intermet.2017.01.007>.
- 567 [60] I. Toda-Caraballo, A general formulation for solid solution hardening effect in
568 multicomponent alloys, *Scr. Mater.* 127 (2017) 113–117.
569 <https://doi.org/10.1016/j.scriptamat.2016.09.009>.
- 570 [61] A. Mishra, G. Priyadarshan, D. Clark, Y. Lu, R. Shi, Theoretical Investigations on Structural
571 Stability and Elastic Properties of MoNbTaW-X (=Ti/V) High Entropy Alloys, 2019.
572 <http://www.sdiarticle4.com/review-history/52208> (accessed October 11, 2020).
- 573 [62] U. Bhandari, C. Zhang, S. Guo, S. Yang, First-principles study on the mechanical and
574 thermodynamic properties of MoNbTaTiW, *Int. J. Miner. Metall. Mater.* 27 (2020) 1398–
575 1404. <https://doi.org/10.1007/s12613-020-2077-1>.
- 576 [63] C.S. Becquart, C. Domain, Ab initio calculations about intrinsic point defects and He in W,
577 *Nucl. Instruments Methods Phys. Res. Sect. B Beam Interact. with Mater. Atoms.* 255 (2007)
578 23–26. <https://doi.org/10.1016/j.nimb.2006.11.006>.
- 579 [64] W.H. He, X. Gao, N. Gao, J. Wang, D. Wang, M.H. Cui, L.L. Pang, Z.G. Wang, Effects of Grain
580 Boundary Characteristics on Its Capability to Trap Point Defects in Tungsten, *Chinese Phys.*
581 *Lett.* 35 (2018) 026101. <https://doi.org/10.1088/0256-307X/35/2/026101>.
- 582 [65] K. Maier, M. Peo, B. Saile, H.E. Schaefer, A. Seeger, High-temperature positron annihilation
583 and vacancy formation in refractory metals, 40 (2006) 701–728.
584 <https://doi.org/10.1080/01418617908234869>.
- 585 [66] P.A. Korzhavyi, I.A. Abrikosov, B.; Johansson, A.; Ruban, H.L. Skriver, First-principles
586 calculations of the vacancy formation energy in transition and noble metals, *Phys. Rev. B.* 59
587 (1999) 11693–11703. <https://doi.org/10.1103/PhysRevB.59.11693>.
- 588 [67] A. Manzoor, Y. Zhang, D.S. Aidhy, Factors affecting the vacancy formation energy in
589 Fe70Ni10Cr20 random concentrated alloy, *Comput. Mater. Sci.* 198 (2021) 110669.
590 <https://doi.org/10.1016/J.COMMATSCI.2021.110669>.
- 591 [68] M.A. Tschopp, K.N. Solanki, F. Gao, X. Sun, M.A. Khaleel, M.F. Horstemeyer, Probing grain
592 boundary sink strength at the nanoscale: Energetics and length scales of vacancy and
593 interstitial absorption by grain boundaries in α -Fe, *Phys. Rev. B - Condens. Matter Mater.*
594 *Phys.* 85 (2012) 064108.
595 <https://doi.org/10.1103/PHYSREVB.85.064108/FIGURES/15/MEDIUM>.
- 596 [69] C.M. Rost, E. Sachet, T. Borman, A. Moballegh, E.C. Dickey, D. Hou, J.L. Jones, S. Curtarolo, J.P.

597 Maria, Entropy-stabilized oxides, Nat. Commun. 2015 61. 6 (2015) 1–8.
598 <https://doi.org/10.1038/ncomms9485>.
599